Proceedings of the Estonian Academy of Sciences,
2023, **72**, 1, 30–40
https://doi.org/10.3176/proc.2023.1.04
Available online at www.eap.ee/proceedings

OPTICS

Performance analysis of WSN–FSO system modeled by Gamma–Chi-square channel distribution

Jelena Todorović[a*], Branimir Jakšić[a], Petar Spalević[a], Miloš Dobrojević[b] and Ivan Milovanović[b]

[a] Faculty of Technical Sciences, University of Pristina in Kosovska Mitrovica, Knjaza Milosa 7, Kosovska Mitrovica, Serbia
[b] Faculty of Technical Sciences, Singidunum University, Danijelova 32, Belgrade, Serbia

Received 4 April 2022, accepted 30 May 2022, available online 27 January 2023

© 2023 Authors. This is an Open Access article distributed under the terms and conditions of the Creative Commons Attribution 4.0 International License CC BY 4.0 (http://creativecommons.org/licenses/by/4.0).

Abstract. This paper presents the WSN–FSO (wireless sensor network–free-space optics) system based on CCR (corner cube retroreflector) and modeled with Gamma–Chi-square distribution. The expressions of ABER (average bit error rate) for the received signal under conditions of different levels of atmospheric turbulence are calculated. Numerical results are presented in the form of graphs, and the results are confirmed by the Monte Carlo simulation. Graphs are presented for different Rician factor values, link lengths, and different levels of atmospheric turbulence. The obtained results are compared with the existing results for other FSO channel distribution models. After thorough consideration we conclude that Gamma–Chi-square gives a better system performance in terms of ABER.

Keywords: ABER (average bit error rate), FSO (free-space optics), WSN (wireless sensor networks), Gamma–Chi-Square.

1. INTRODUCTION

With the development of wireless communications, there is a growing interest in the development of wireless sensor networks (WSNs) for various applications. WSNs offer reliable, low-power and low-cost platforms that connect the physical environment with management and information systems to provide advanced monitoring and control solutions for a wide range of applications [1]. There are many advantages of WSNs, such as autonomous distributed control, self-organization, network scalability, simplicity of setting, greater flexibility in design [2,3].

The WSN also has some disadvantages when using radio frequency (RF) channel for communications, such as limited bandwidth resources, electromagnetic interference, easy signal interception and high energy consumption [3–5]. In order to avoid the abovementioned problems, the use of free-space optics (FSO) technology for wireless signal transmission is explored, which due to its numerous advantages can be a good solution [6,7]. FSO communication systems offer a license-free and cost-effective access performance, high data rate, highly secured, extremely large bandwidth and simplicity of system design and implementation [8]. However, the major limitation of FSO performance is the atmospheric turbulence, which originates from variations in the refractive index of the transmission medium due to temperature inhomogeneity and pressure changes [9–11].

* Corresponding author, jelena.todorovic@pr.ac.rs

A WSN consists of a large number of small networked sensor nodes that are deployed to sense, process data, and communicate with the rest of the system. Due to restrictions in the node size, there are limitations in the energy resources, memory and throughput of the sensor itself. Numerous applications of WSNs are constrained by the limited battery power of the sensor; therefore, the primary goal is to improve the energy efficiency of the sensor. Since in some environments it is very difficult or not possible to replace or recharge the batteries, and the network lifetime is determined by the lifetime of the battery, energy efficiency is one of the main issues [1,4].

In order to improve the energy efficiency of the sensor, a passive optical retroreflector known as corner cube retroreflector (CCR) is often used in WSN–FSO systems. It is characterized by small size, ease of operation and negligible energy consumption, so it is highly suitable for use in such systems. An ideal CCR consists of three mutually orthogonal mirrors that form a concave corner. A continuous laser beam is emitted towards each node. When the light beam enters the CCR, it bounces off each of the three mirrors and reflects back toward the source parallel to the direction it entered. The decision of the corresponding node is detected based on the intensity of the reflected beam. If the decision is 1, CCR reflects the laser beam back, while if the decision is 0, CCR will not be activated and no signal will be reflected, which indicates lower energy consumption [4,12,13].

Numerous papers deal with the issue of WSNs and their application and analysis in various systems including FSO [3,14–19]. In [3] a scheme for solving the problem of analyzing the power efficiency based on node positioning in optical WSN is proposed. Location estimation and detection in the presence of fading were analyzed in [14]. The paper [17] studies an energy heterogeneous WSN, where nodes can cooperate with each other to improve the energy efficiency of the network. In paper [19] the hybrid RF/FSO WSN model was proposed with the aim of reducing energy consumption. In [2], the optical WSN system and its performance when using CCR were analyzed. The research is quite focused on the work and application of CCR. The ultrasonic reflective characteristics of a CCR are investigated in [20], while flexible CCR array for temperature and strain sensing is considered in [21]. Other models of retroreflectors that represent the modifications of CCR created in order to improve the performance given in [22,23].

Motivated by the above issues, in this paper we have analyzed the performance of the WSN–FSO system based on CCR by observing the OOK (on-off keying) modulated signal through the ABER behavior. The WSN–FSO system is observed in different atmospheric turbulence strength level conditions over novel Gamma–Chi-square turbulence model. To the best of the authors' knowledge, there are no similar analyses or results presented in the available literature.

The main contributions of this paper are:

- Analytical expressions for the ABER of the received signal in the WSN–FSO system based on CCR operating in conditions of different atmospheric turbulence strength levels over novel Gamma–Chi-square turbulence model.
- Numerical results are presented in the form of graphs, and the results are confirmed by the Monte Carlo simulation. The obtained results are compared with the existing results for other channel distributions.
- Based on the obtained results, the behavior of FSO channel in different atmospheric turbulence conditions can be predicted for different values of network parameters. In that way we have provided lower and higher bound approximation for FSO transmission in different turbulence conditions. This could enable the designers of wireless optical systems to create rational solutions for the desired system performance.

The paper is organized as follows. Section 2 describes the WSN–FSO system with novel Gamma–Chi-square channel distribution model. In Section 3, the initial expressions for the ABER calculation are given and analytical closed-form expression for ABER is derived and presented. The numerical results obtained for different levels of atmospheric turbulence and FSO link distance are presented and discussed in Section 4. The conclusions are highlighted in Section 5.

2. SYSTEM MODEL

The laser emits an optical beam towards the CCR nodes with a transmitting power P_t and semiangle of illuminated field θ_f. Average power reflected by the n-th CCR is expressed as [2,4]:

$$P_{c,n} = \frac{P_t d_c^2 \cos^2 \theta_{s,n} \cos \theta_{c,n} R_c}{8L^2 \tan^2 \theta_f}, \tag{1}$$

where d_c is the effective diameter of the CCR, $\theta_{s,n}$ is the angle between the laser and the axis of the link, $\theta_{c,n}$ represents the angle between the center of the laser beam and the axis of the link, R_c signifies the effective reflectivity of the CCR, and L is horizontal distance between the laser and the n-th CCR. The diffracted irradiance at the lens reflected by the n-th CCR is given as:

$$I_{l,n} = \frac{P_{c,n} \pi d_c^2 \cos^2 \theta_{s,n} \cos \theta_{l,n}}{4\lambda^2 L^2}, \tag{2}$$

where $\theta_{l,n}$ represents the angle between the direction to the camera lens and the axis of the link and λ is the laser wavelength. The average received photocurrent reflected by the n-th CCR is given by:

$$i_{r,n} = \frac{I_{l,n} \pi d_l^2 T_l T_f f_{act} R}{4}, \tag{3}$$

where d_l represents the effective diameter of the camera lens, T_l is the transmission efficiency of the camera lens, T_f signifies the optical filter transmission efficiency, f_{act} is the active fraction of the camera pixel area, and R is the pixel responsivity.

Finally, the received power at the photodetector is given by:

$$P_{r,n} = i_{r,n}^2, \tag{4}$$

and the received signal at the FC (fusion center) reflected from the n-th node is given as:

$$y_n = \sqrt{P_{r,n}} hgx_n + w_n, \tag{5}$$

where x_n represents the local binary decision of the node n. As the distance between the transmitter and the receiver is considered large enough, h and g represent the independent channels of atmospheric turbulence between the transmitter and the CCR and between the CCR and the receiver, respectively. Parameter w_n is the additive noise at the input of the receiver camera of the FC, which includes the ambient light shot noise and the thermal noise, where the total noise variance, σ^2 is:

$$\sigma^2 = \left(S_{bg} + S_R\right) R_b, \tag{6}$$

and R_b represents the bit rate. The one-sided power spectral density of the shot noise due to the ambient light is $S_{bg} = 2qi_{bg}$, where q is the electron charge and i_{bg} is the photocurrent per pixel due to the ambient light given by:

$$i_{bg,n} = \frac{\pi p_{bg} R_{bg} \Delta\lambda \tan^2 \theta_f d_l^2 T_l T_f f_{act} R}{4N_p}. \tag{7}$$

The parameter p_{bg} represents the power spectral density of the ambient light that illuminates the area around the CCR and this area reflects the ambient light with reflectivity R_{bg}, $\Delta\lambda$ signifies the bandwidth of the optical bandpass filter, and Np is the number of pixels in the image sensor.

The load resistance R_F depends on the thermal noise having power spectral density given by:

$$S_R = \frac{4k_B T}{R_F}, \tag{8}$$

where k_B is the Boltzmann constant and T is the absolute temperature.

Distribution used to describe h and g channels, i.e., atmospheric turbulence channel between transmitter and CCR, as well as between CCR and receiver is the novel Gamma–Chi-square irradiance PDF (probability density function) model given as [24]:

$$f_I(I) = \sum_{m=0}^{\infty} \frac{2K^m \mathrm{e}^{-K}}{\Gamma(\alpha)\Gamma(m+1)m!} \left(\frac{\alpha(1+K)}{\Omega_P} \right)^{\frac{\alpha+m+1}{2}} I^{\frac{\alpha+m-1}{2}} K_{\alpha-m-1}\left(2\sqrt{\frac{\alpha(1+K)}{\Omega_P} I} \right), \tag{9}$$

where I is irradiance at the receiver, $\Gamma(\cdot)$ represents the Gamma function [25, Eq. 8.310], and $K\upsilon(\cdot)$ υth-order modified Bessel function of the second kind [25, Eq. 8.432]. The parameter K is the ratio of the power of the LOS (line of sight) component to the average power of the scattered component [26], and Ω_P represents the total received signal power. The parameter α is the atmospheric turbulence parameter that represents the effective number of small-scale eddies of the scattering environment. This is the parameter of atmospheric turbulence that for propagation of plane waves and zero inner scale can be expressed as [24]:

$$\alpha = \left[\mathrm{e}^{\frac{0.49\sigma_R^2}{\left(1+1.11\sigma_R^{12/5}\right)^{7/6}}} - 1 \right]^{-1}, \tag{10}$$

where σ_R^2 represents the Rytov variance used to determine the intensity of the optical signal due to atmospheric turbulence, and is defined as:

$$\sigma_R^2 = 1.23 C_n^2 k^{7/6} L^{11/6}. \tag{11}$$

The parameter C_n^2 denotes the index of refraction used as a measure of the turbulence strength. For the horizontal propagation path, the parameter C_n^2 is considered constant with mean values from 10^{-17} m$^{-2/3}$ to 10^{-13} m$^{-2/3}$ for channels from weak to strong turbulence, respectively. The parameter k is an optical wave number, defined as $k=2\pi/\lambda$ with wavelength λ, while L denotes the distance between the transmitter and the receiver, i.e., the length of the optical signal propagation.

3. ANALYTICAL RESULTS

The ABER for an optical signal transmitted by the previously described WSN–FSO system with the OOK modulation scheme can be expressed as [4]:

$$P_e = \frac{1}{\pi} \int_0^{\pi/2} \int_0^{\infty} \int_0^{\infty} e^{-\tau h^2 g^2} f(h) f(g) \cdot dh dg d\theta, \tag{12}$$

where $\tau = \dfrac{P_r}{8\sigma^2 \sin^2 \theta}$.

Since the observed system is modeled with two independent channels of atmospheric turbulence, (12) can be simplified as:

$$P_e = \frac{1}{\pi} \int_0^{\pi/2} I_g \cdot d\theta, \tag{13}$$

where I_g is represented as:

$$I_g = \int_0^\infty I_h f(g) \cdot dg\,, \tag{14}$$

while I_h is given as:

$$I_h = \int_0^\infty e^{-\tau h^2 g^2} f(h) \cdot dh\,. \tag{15}$$

Therefore, in order to derive closed-form expression for ABER, I_h (15) is first calculated, the solution of which is substituted in (14), in order to obtain I_g. The obtained solution of the integral for (14) is further substituted in (13), the solution of which gives the required ultimate expression.

In order to derive the final solution, the modified Bessel function of the second kind can be represented by the Fox function as follows [27, Eq. 2.9.19]:

$$H_{0,2}^{2,0}\left[\frac{z^2}{4}\middle|\begin{matrix}-\\ \left(\frac{a-\eta}{2},1\right),\ \left(\frac{a+\eta}{2},1\right)\end{matrix}\right] = 2\left(\frac{z}{2}\right)^a K_\eta(z)\,, \tag{16}$$

thus, the Gamma–Chi-square irradiance PDF model from (9) reduces to:

$$f_I(I) = \sum_{m=0}^{\infty} \frac{K^m \mathrm{e}^{-K}}{\Gamma(\alpha)\Gamma(m+1)m!} \frac{\alpha(1+K)}{\Omega_P} H_{0,2}^{2,0}\left[\frac{\alpha(1+K)}{\Omega_P} I\middle|\begin{matrix}-\\ (m,1),\ (\alpha-1,1)\end{matrix}\right]. \tag{17}$$

By substituting (17) into (15) we obtain:

$$I_h = \sum_{m=0}^{\infty} \frac{K^m \mathrm{e}^{-K}}{\Gamma(\alpha)\Gamma(m+1)m!} \frac{\alpha(1+K)}{\Omega_P} \int_0^\infty e^{-\tau g^2 h^2} H_{0,2}^{2,0}\left[\frac{\alpha(1+K)}{\Omega_P} h\middle|\begin{matrix}-\\ (m,1),\ (\alpha-1,1)\end{matrix}\right] dh\,, \tag{18}$$

where $e^{-\tau g^2 h^2}$ can also be represented by the Fox function as [27, Eq. 2.9.4]:

$$H_{0,1}^{1,0}\left[z\middle|\begin{matrix}-\\ (b,\beta)\end{matrix}\right] = \frac{1}{\beta} z^{b/\beta} e^{-z^{1/\beta}}. \tag{19}$$

Thus, the I_h form now is:

$$I_h = \sum_{m=0}^{\infty} \frac{K^m \mathrm{e}^{-K}}{2\Gamma(\alpha)\Gamma(m+1)m!} \frac{\alpha(1+K)}{\Omega_P} \int_0^\infty H_{0,1}^{1,0}\left[\sqrt{\tau} g h\middle|\begin{matrix}-\\ \left(0,\frac{1}{2}\right)\end{matrix}\right] H_{0,2}^{2,0}\left[\frac{\alpha(1+K)}{\Omega_P} h\middle|\begin{matrix}-\\ (m,1),\ (\alpha-1,1)\end{matrix}\right] dh\,. \tag{20}$$

By applying [28, Eq. 2.25.1.1] a solution is obtained for a given integral in (20):

$$I_h = \sum_{m=0}^{\infty} \frac{K^m \mathrm{e}^{-K}}{2\Gamma(\alpha)\Gamma(m+1)m!} \frac{\alpha(1+K)}{\Omega_P} \frac{1}{\sqrt{\tau} g} H_{1,2}^{2,1}\left[\frac{\alpha(1+K)}{\Omega_P \sqrt{\tau} g}\middle|\begin{matrix}\left(\frac{1}{2},\frac{1}{2}\right)\\ (m,1),\ (\alpha-1,1)\end{matrix}\right], \tag{21}$$

which based on [27, Eq. 2.1.3]

$$H_{p,q}^{m,n}\left[\frac{1}{z}\middle|\begin{matrix}(a_i,\alpha_i)_{1,p}\\(b_j,\beta_j)_{1,q}\end{matrix}\right]=H_{q,p}^{n,m}\left[z\middle|\begin{matrix}(1-b_j,\beta_j)_{1,q}\\(1-a_i,\alpha_i)_{1,p}\end{matrix}\right], \tag{22}$$

can be rewritten as:

$$I_h=\sum_{m=0}^{\infty}\frac{K^m\,\mathrm{e}^{-K}}{2\Gamma(\alpha)\Gamma(m+1)m!}\frac{\alpha(1+K)}{\Omega_P}\frac{1}{\sqrt{\tau g}}H_{2,1}^{1,2}\left[\frac{\Omega_P\sqrt{\tau g}}{\alpha(1+K)}\middle|\begin{matrix}(1-m,1),\ (2-\alpha,1)\\(\frac{1}{2},\frac{1}{2})\end{matrix}\right]. \tag{23}$$

By substituting (23) and (17) into (14), I_g is obtained as:

$$I_g=\sum_{m=0}^{\infty}\sum_{n=0}^{\infty}\frac{K^mK^n}{2\Gamma(m+1)\Gamma(n+1)m!n!\sqrt{\tau}}\left(\frac{\alpha(1+K)\mathrm{e}^{-K}}{\Omega_P\Gamma(\alpha)}\right)^2\cdot \int_0^{\infty}g^{-1}H_{2,1}^{1,2}\left[\frac{\Omega_P\sqrt{\tau}}{\alpha(1+K)}g\middle|\begin{matrix}(1-m,1),\ (2-\alpha,1)\\(\frac{1}{2},\frac{1}{2})\end{matrix}\right]H_{0,2}^{2,0}\left[\frac{\alpha(1+K)}{\Omega_P}g\middle|\begin{matrix}-\\(n,1),\ (\alpha-1,1)\end{matrix}\right]dg, \tag{24}$$

whose solution is reached by using [28, Eq. 2.25.1.1]:

$$I_g=\sum_{m=0}^{\infty}\sum_{n=0}^{\infty}\frac{K^mK^n}{2\Gamma(m+1)\Gamma(n+1)m!n!\sqrt{\tau}}\left(\frac{\alpha(1+K)\mathrm{e}^{-K}}{\Omega_P\Gamma(\alpha)}\right)^2\cdot H_{1,4}^{4,1}\left[\frac{\alpha^2(1+K)^2}{\Omega_P^2\sqrt{\tau}}\middle|\begin{matrix}(\frac{1}{2},\frac{1}{2})\\(n,1),\ (\alpha-1,1),\ (m,1),\ (\alpha-1,1)\end{matrix}\right]. \tag{25}$$

In order to derive the closed-form expression for ABER, the solution obtained in (25) is substituted in (13):

$$P_e=\sum_{m=0}^{\infty}\sum_{n=0}^{\infty}\frac{K^mK^n}{2\pi\Gamma(m+1)\Gamma(n+1)m!n!}\left(\frac{\alpha(1+K)\mathrm{e}^{-K}}{\Omega_P\Gamma(\alpha)}\right)^2\cdot \int_0^{\pi/2}\frac{1}{\sqrt{\tau}}H_{1,4}^{4,1}\left[\frac{\alpha^2(1+K)^2}{\Omega_P^2\sqrt{\tau}}\middle|\begin{matrix}(\frac{1}{2},\frac{1}{2})\\(n,1),\ (\alpha-1,1),\ (m,1),\ (\alpha-1,1)\end{matrix}\right]d\theta. \tag{26}$$

The parameter τ can be represented as $\tau=\varphi/\omega$, where $\varphi=P_r/(8\sigma^2)$ and $\omega\sin^2\theta$. After their substitution, (26) can be rewritten as:

$$P_e=\sum_{m=0}^{\infty}\sum_{n=0}^{\infty}\frac{K^mK^n}{4\pi\Gamma(m+1)\Gamma(n+1)m!n!\sqrt{\varphi}}\left(\frac{\alpha(1+K)\mathrm{e}^{-K}}{\Omega_P\Gamma(\alpha)}\right)^2\cdot \int_0^{1}(1-\omega)^{-\frac{1}{2}}H_{1,4}^{4,1}\left[\frac{\alpha^2(1+K)^2}{\Omega_P^2\sqrt{\varphi}}\omega^{\frac{1}{2}}\middle|\begin{matrix}(\frac{1}{2},\frac{1}{2})\\(n,1),\ (\alpha-1,1),\ (m,1),\ (\alpha-1,1)\end{matrix}\right]d\omega. \tag{27}$$

By employing the solution of the resulting integral given by [28, Eq. 2.25.2.2], we derive the ABER closed-form expression for the Gamma–Chi-square channel model as follows:

$$P_e = \sum_{m=0}^{\infty}\sum_{n=0}^{\infty} \frac{K^m K^n}{4\pi\Gamma(m+1)\Gamma(n+1)m!n!\sqrt{\varphi}} \left(\frac{\alpha(1+K)\mathrm{e}^{-K}}{\Omega_P \Gamma(\alpha)}\right)^2 \cdot H_{3,5}^{4,3}\left[\left(\frac{\alpha(1+K)}{\Omega_P}\right)^2 \frac{1}{\sqrt{\varphi}} \middle| \begin{matrix} \left(0,\frac{1}{2}\right),\left(\frac{1}{2},0\right),\left(\frac{1}{2},\frac{1}{2}\right) \\ (n,1),\ (\alpha-1,1),\ (m,1),\ (\alpha-1,1),\left(-\frac{1}{2},\frac{1}{2}\right) \end{matrix}\right]. \quad (28)$$

4. NUMERICAL RESULTS

Based on the calculated closed-form expression for ABER (28), numerical and graphical results were obtained describing the ABER behavior for different values of system parameters. Additionally, analytical results were verified by the Monte Carlo simulation.

In the final solution of the analytical expression for ABER (28), the Fox function appears, which is defined by the Mellin–Barnes type integral with the integrand containing products and quotients of the Euler Gamma functions. The Fox function generalizes most special functions and it can be developed in the form of integrals of different products [27,29,30]. MATLAB, Wolfram Mathematica and other software tools do not have the ability to directly calculate the Fox function, and program codes must be created for its software implementation. There are several published program codes that evaluate the Fox function [30]. Using [27,29–31] and by modification, numerical values for expression (28) were obtained.

The values of the system parameters are given in Table 1 [2,4].

Figure 1 shows the ABER behavior depending on the average transmitted optical power P_t for different values of the FSO link length (L = 500 m, L = 1000 m and L = 2000 m), different strength levels of atmospheric turbulence (strong $C_n^2 = 1.2\times10^{-13}$, moderate $C_n^2 = 2\times10^{-14}$ and weak $C_n^2 = 6\times10^{-15}$) and for a fixed value of Rician factor K = 1. From the given graphs it can be seen that ABER decreases with increasing average signal power. The fastest decrease of ABER is achieved with weak atmospheric turbulence and the slowest with strong atmospheric turbulence. It is evident that as the length of the FSO link decreases, so do the ABER values. At lower power values, there is almost no difference in ABER values for different FSO link lengths. The impact of the FSO link length is more pronounced with an increase in the average signal power.

Figures 2, 3, and 4 depict the ABER behavior depending on the average transmitted signal power for strong, moderate and weak atmospheric turbulence, respectively. Graphs for different values of the K factor at FSO link length of L = 1000 m are given. From the given graphs, it can be concluded that with the increase

Table 1. System parameters

Parameter	Value	Parameter	Value
N	10	P_o	0.5
p_d	0.5	p_f	0.1
R_c	0.85	T_l	0.1
d_c	0.0005	d_l	0.1
Tf	0.8	$fact$	0.75
R	0.5	θ_c	60°
θ_s	60°	θ_l	60°
λ	830×10^{-9}	θ_f	1°
R_b	103	K_b	1.38×10^{-23}
T	300	R_f	20×10^6
P_{bg}	0.8	R_{bg}	0.3
$\Delta\lambda$	5×10^{-9}	N_p	10^5
q	$1.6021765 \times 10^{-19}$		

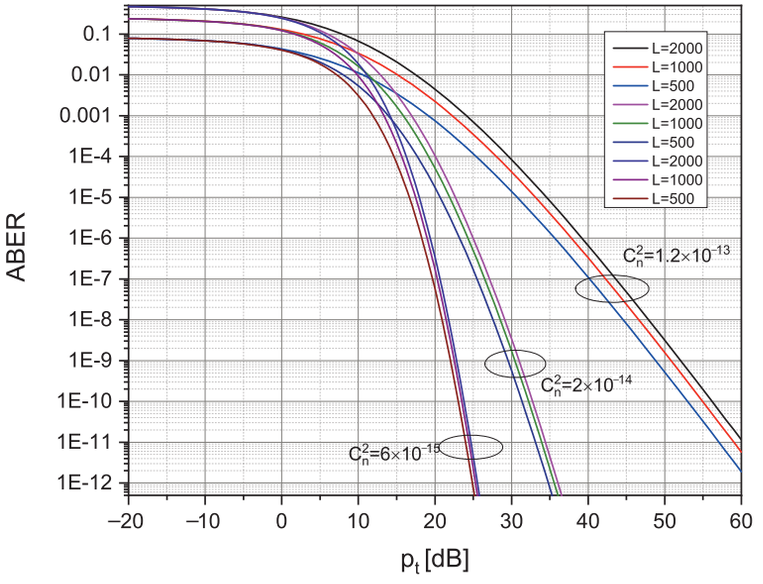

Fig. 1. ABER for different levels of atmospheric turbulence and FSO link distance.

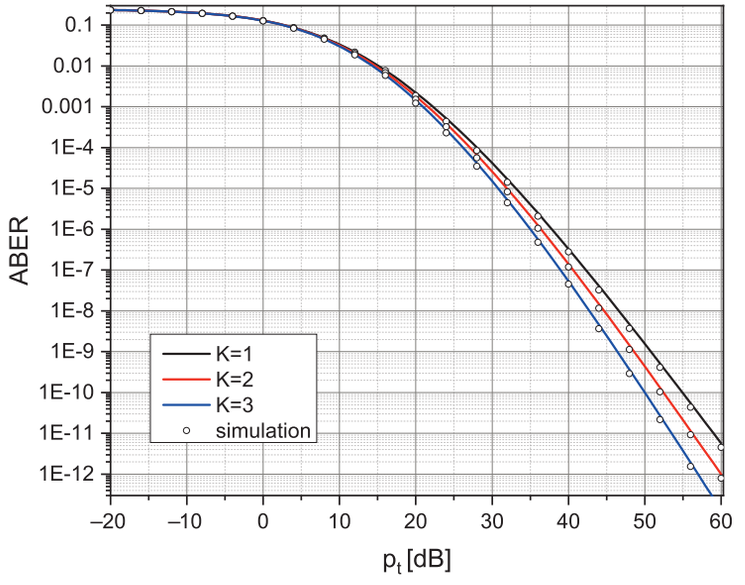

Fig. 2. ABER for different *K* factor values in strong atmospheric turbulence.

of the *K* factor, the system performance improves, i.e., lower ABER values are obtained. Further, the *K* factor at low values of average power does not affect the communication system performance – ABER has approximately the same value for all values of the *K* factor. The results obtained by the Monte Carlo simulation coincide with the numerical results obtained on the basis of expression (28).

If the obtained ABER results for the Gamma–Chi-Square channel model are compared with the ABER results obtained for other FSO channel models [4], it is obvious that the Gamma–Chi-Square model gives a better performance in terms of ABER values. Lower ABER values are obtained for the same parameters of the FSO communication system.

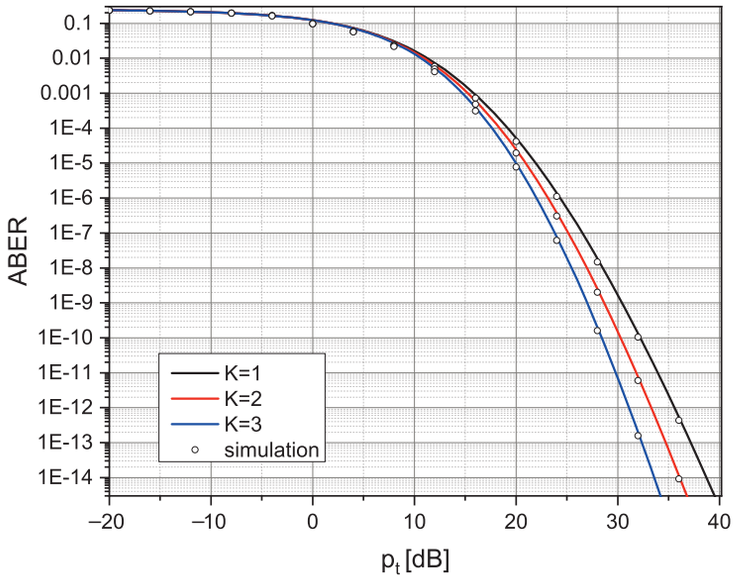

Fig. 3. ABER for different K factor values in moderate atmospheric turbulence.

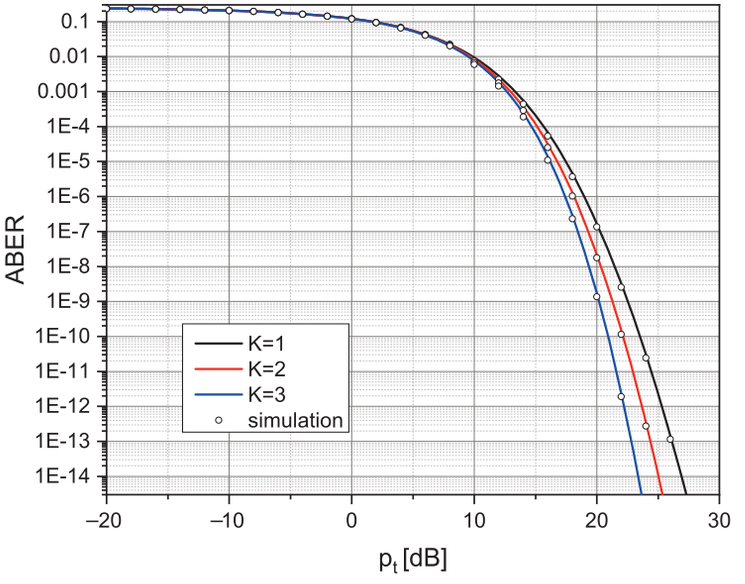

Fig. 4. ABER for different K factor values in weak atmospheric turbulence.

Figure 5 shows the ABER behavior depending on the FSO link length and for different strength levels of atmospheric turbulence (Rician factor $K = 1$ and the average transmitted optical power $P_t = 20$ dB).

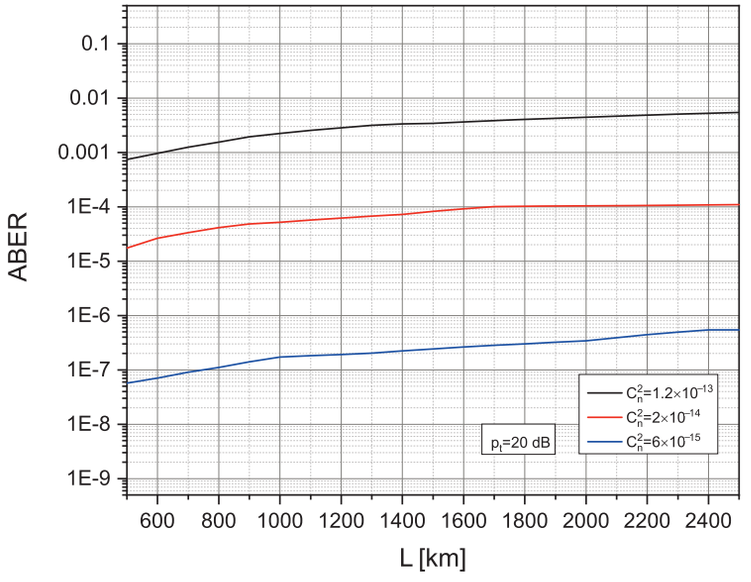

Fig. 5. ABER for different FSO link length.

5. CONCLUSIONS

The paper presents the WSN–FSO system based on CCR and modeled with Gamma–Chi-square distribution. The obtained ABER values for modulated signals by OOK modulation scheme are presented and analyzed. The WSN–FSO system was observed for different levels of atmospheric turbulence and different FSO link distances, as well as for other system parameters. Based on the obtained results, it is evident that the system performs best in weak atmospheric turbulence conditions and for shorter link distances. The impact of the FSO link length is more pronounced with the increase of the average signal power, while for lower power values there is almost no difference. In addition, the impact of the *K* factor on system performance is shown. It can be seen that increasing the *K* factor improves the quality of transmission. At lower power values, changes in the *K* factor do not significantly affect the transmission, because ABER has almost the same values. Besides, comparing the results obtained in this paper with the results obtained for other FSO distribution models, it can be concluded that Gamma–Chi-square gives better system performance in terms of ABER.

The obtained results can be used in the design of WSN–FSO systems to create rational solutions for the desired system performance, in order to obtain the highest quality of signal reception.

ACKNOWLEDGEMENT

The publication costs of this article were partially covered by the Estonian Academy of Sciences.

REFERENCES

1. Shammaa, S. and Verma, P. Interconnection of IEEE 802.15.4 islands through free space optical communication links. In *Proceedings of the 5th International Conference on Signal Processing and Communication Systems (ICSPCS), Honolulu, USA, 12–14 December, 2011*. IEEE, 2012, 1–9. https://doi.org/10.1109/icspcs.2011.6140892
2. Teramoto, S. and Ohtsuki, T. Optical wireless sensor network system using corner cube retroreflectors (CCRs). In *Proceedings of the IEEE Global Telecommunications Conference (GLOBECOM), Dallas, USA, 29 November – 3 December 2004*. IEEE, 2004, 1035–1039. https://doi.org/10.1109/glocom.2004.1378115

3. Yan, Z., Mukherjee, A., Yang, L., Routray, S. and Palai, G. Energy-efficient node positioning in optical wireless sensor networks. *Optik*, 2019, **178**, 461–466. https://doi.org/10.1016/j.ijleo.2018.09.186
4. Althunibat, S., Altarawneh, Z. and Mesleh, R. Performance analysis of free space optical-based wireless sensor networks using corner cube retroreflectors. *Trans. Emerg. Telecommun. Technol.*, 2019, **30**(12), e3707. https://doi.org/10.1002/ett.3707
5. Babic, R. *Analiza signala (Signal Analysis)*. Akademska Misao, Belgrade, 2000 (in Serbian).
6. Badarneh, O. S., Derbas, R., Almehmadi, F. S., El Bouanani, F. and Muhaidat, S. Performance analysis of FSO communications over F turbulence channels with pointing errors. *IEEE Commun. Lett.*, 2021, **25**(3), 926–930. https://doi.org/10.1109/lcomm.2020.3042489
7. Ndjiongue, A. R., Ngatched, T., Dobre, O., Armada, A. G. and Haas, H. Analysis of RIS-based terrestrial-FSO link over G-G turbulence with distance and jitter ratios. *J. Light. Technol.*, 2021, **39**(21), 6746–6758. https://doi.org/10.1109/JLT.2021.3108532
8. Stefanovic, C., Morales-Céspedes, M. and Armada, A. G. Performance analysis of RIS-assisted FSO communications over Fisher–Snedecor F turbulence channels. *Appl. Sci.*, 2021, **11**(21), 10149. https://doi.org/10.3390/app112110149
9. Amirabadi, M. A., Kahaei, M. H. and Nezamalhosseini, S. A. Deep learning based detection technique for FSO communication systems. *Phys. Commun.*, 2020, **43**, 101229. https://doi.org/10.1016/j.phycom.2020.101229
10. Jahid, A., Alsharif, M. H. and Hall, T. J. A contemporary survey on free space optical communication: potential, technical challenges, recent advances and research direction. *J. Netw. Comput. Appl.*, 2022, **200**, 103311. https://doi.org/10.1016/j.jnca.2021.103311
11. Trung, H. D., Hoa, N. T., Trung, N. H. and Ohtsuki, T. A closed-form expression for performance optimization of subcarrier intensity QAM signals-based relay-added FSO systems with APD. *Phys. Commun.*, 2018, **31**, 203–211. https://doi.org/10.1016/j.phycom.2018.04.012
12. Won, J., Oh, Y., Park, J., Park, J. Y., Jo, M.-S. and Kim, D. Development and characterization of piezoelectrically actuated corner cube retroreflectors for applications in free-space optical sensor network. *Appl. Opt.*, 2012, **51**(13), 2315–2321. https://doi.org/10.1364/AO.51.002315
13. Yang, G., You, S., Bi, M., Fan, B., Lu, Y., Zhou, X. et al. Wave-optics simulation of the double-pass beam propagation in modulating retro-reflector FSO systems using a corner cube reflector. *Appl. Opt.*, 2017, **56**(26), 7474–7483. https://doi.org/10.1364/AO.56.007474
14. Zhang, X., Tepedelenlioğlu, C., Banavar, M. K., Spanias, A. and Muniraju, G. Location estimation and detection in wireless sensor networks in the presence of fading. *Phys. Commun.*, 2019, **32**, 62–74. https://doi.org/10.1016/j.phycom.2018.10.010
15. Huang, J. and Li, Z. Infrared-based short-distance FSO sensor network system. *Int. J. Online and Biomedical Engineering (iJOE)*, 2018, **14**(12), 43–56. https://doi.org/10.3991/ijoe.v14i12.9493
16. Kumar, L., Sharma, V. and Singh, A. Cluster-based single-sink wireless sensor networks and passive optical network converged network incorporating sideband modulation schemes. *Opt. Eng.*, 2018, **57**(2), 026102. https://doi.org/10.1117/1.OE.57.2.026102
17. Liang, J., Xu, Z., Xu, Y., Zhou, W. and Li, C. Adaptive cooperative routing transmission for energy heterogeneous wireless sensor networks. *Phys. Commun.*, 2021, **49**, 101460. https://doi.org/10.1016/j.phycom.2021.101460
18. Yu, H. and Zikria, Y. B. Cognitive radio networks for Internet of Things and wireless sensor networks. *Sensors*, 2020, **20**(18), 5288. https://doi.org/10.3390/s20185288
19. Sivathasan, S. and O'Brien, D. Hybrid radio and optical communications for energy-efficient wireless sensor networks, *IETE J. Res.*, 2011, **57**(5), 396–406.
20. Ploix, M.-A., Kauffmann, P., Chaix, J.-F., Lillamand, I., Baqué, F. and Corneloup, G. Acoustical properties of an immersed corner-cube retroreflector alone and behind screen for ultrasonic telemetry applications. *Ultrasonics*, 2020, **106**, 106149. https://doi.org/10.1016/j.ultras.2020.106149
21. Khalid, M. W., Ahmed, R., Yetisen, A. K. and Butt, H. Flexible corner cube retroreflector array for temperature and strain sensing. *RSC Adv.*, 2018, **14**, 7588–7598. https://doi.org/10.1039/c7ra13284k
22. Lewellen, J. W. and Harris, J. R. Performance estimates for a multicube retroreflector design. *Opt. Commun.*, 2019, **441**, 26–32. https://doi.org/10.1016/j.optcom.2019.02.013
23. Rosenkrantz, E. and Arnon, S. 1550 nm modulating retroreflector based on coated nanoparticles for free-space optical communication. *Appl. Opt.*, 2015, **54**(17), 5309–5313. https://doi.org/10.1364/ao.54.005309
24. Todorović, J., Spalević, P., Panić, S., Milosavljević, B. and Gligorijević, M. FSO system performance analysis based on novel Gamma–Chi-square irradiance PDF model. *Opt. Appl.*, 2021, **51**(3), 335–348. https://doi.org/10.37190/oa210303
25. Gradshteyn, I. S. and Ryzhik, I. M. *Table of Integrals, Series, and Products*. 7th ed. Elsevier Academic Press, USA, 2007.
26. Belmonte, A. and Kahn, J. M. Performance of synchronous optical receivers using atmospheric compensation techniques. *Opt. Express*, 2008, **16**(18), 14151–14162. https://doi.org/10.1364/oe.16.014151
27. Kilbas, A. A. and Saigo, M. *H-Transforms Theory and Applications*. Chapman & Hall / CRC Press, USA, 2004.
28. Prudnikov, A. P., Brychkov, Y. A. and Marichev, O. I. *Интегралы и ряды (Integrals and Series)*. 2nd ed. Fizmatlit, Moscow, 2003 (in Russian).
29. Chergui, H., Benjillali, M. and Alouini, M.-S. *Technical Report: Rician K-Factor-Based Analysis of XLOS Service Probability in 5G Outdoor Ultra-Dense Networks*. Cornell University, New York, 2018. https://doi.org/10.48550/arXiv.1804.08101
30. Coelho, C. A. and Arnold, B. *Finite Form Representations for Meijer G and Fox H Functions: Applied to Multivariate Likelihood Ratio Tests Using Mathematica*. Springer, Cham, 2019.
31. Al-Omari, S. K. Extension of generalized Fox's H-function operator to certain set of generalized integrable functions. *Adv. Differ. Equ.*, 2020, **2020**, 448. https://doi.org/10.1186/s13662-020-02910-8